Competition between CoOx and CoPt phases in Pt/Co/AlOx semi tunnel junctions

Houmed Garad, Luc Ortega, Aline Y. Ramos, Yves Joly, Farid Fettar, Stephane Auffret, Bernard Rodmacq, Bernard Dieny, Olivier Proux, A.I. Erko

Competition between CoO_x and CoPt phases in Pt/Co/AlO_x semi tunnel junctions

H. Garad,[1,a)] L. Ortega,[1] A. Y. Ramos,[1] Y. Joly,[1] F. Fettar,[1] S. Auffret,[2] B. Rodmacq,[2] B. Diény,[2] O. Proux,[3] and A. I. Erko[4]

[1]*Institut Néel, CNRS & Université Joseph Fourier, BP166, F-38042 Grenoble Cedex 9, France*
[2]*SPINTEC, UMR 8191 CEA-CNRS-UJF, 38054 Grenoble Cedex, France*
[3]*Observatoire des Sciences de l'Univers de Grenoble, 414 rue de la Piscine, F-38400 Saint Martin d'Hères, France*
[4]*Helmholtz-Zentrum Berlin für Materialien und Energie, Albert-Einstein Strasse 15, D-12489 Berlin, Germany*

We report on the evolution of the structure and composition of a Pt(3 nm)/Co(0.6 nm)/AlO_x(2 nm) trilayer sputtered on Si/SiO_2 under oxidation and annealing processes by combined x-ray reflectivity and x-ray absorption studies. We describe the progressive and inhomogeneous oxidation of the layers by increasing the oxidation time. Before annealing, the layers have lower density than bulk samples and noticeable roughness. After thermal annealing, a significant improvement of the quality of the alumina layer goes along with the formation of a CoPt alloy that reduces the number of Co-O bonds. These structural outcomes clarify the evolution of the magnetic and transport properties reported at room temperature in these samples. © 2013 AIP Publishing LLC. [http://dx.doi.org/10.1063/1.4816620]

I. INTRODUCTION

The industrial applications of magnetic tunnel junctions (MTJs)[1] in magnetic read-heads,[2] or in magnetic random access memories,[3] impulse a strong research activity. One of the challenging points is the tunneling transport coming from the spin-dependent interfacial density of states and the electronic states within the barrier.[4]

MTJs consist of a thin insulating layer (typically AlO_x (Ref. 5) or MgO_x (Ref. 6)) inserted between two ferromagnetic layers. Such a barrier can be made by deposition of a pure element (Al or Mg) followed by a natural or plasma oxidation. Alternatively, the oxide can be directly deposited starting from an alloyed material. The physical properties of these systems depend strongly on the characteristic buildings, and both oxidation and annealing process. High tunneling magnetoresistance ratios, i.e., variations of the resistance with the magnetic field, are measured at room temperature: 81% (Ref. 7) and 472% (Ref. 8) after annealing at 538 and 723 K, for Al_2O_3 and MgO, respectively. Other systems, based on ferromagnetic layers and complex oxides,[9] are also very promising, because of the positive or negative Co spin polarization induced by the different bonding effects at the interface. At the interface of the barrier, some natural defects[10] also appear during the deposition, and others imperfections are caused by the oxidation conditions.[11,12] The optimization of the oxidation process, controlled by the deposition parameters, for instance, without oxidizing the adjacent magnetic layers[13,14] appears to be essential.

The structural and physical characteristics of tunnel junctions as a function of the oxidation process have already been extensively investigated. Besides techniques dedicated to magnetic and transport measurements,[15] those commonly used are cross-sectional high resolution electron microscopy,[16] *in situ* differential ellipsometry measurements coupled to x-ray photoelectron spectroscopy (XPS),[17] ac impedance,[18] photoconductance,[19] soft x-ray absorption.[20] All these techniques have some of the following drawbacks: (1) study limited at the top layers, buried layers are not investigated, (2) necessity of high vacuum environment, (3) induced destruction of the sample, (4) difficulty to reach a sub-nanometric resolution for very thin layers (some angstroms), and (5) determination of the thicknesses of the layers but without additional pertinent structural parameters, as the roughness or the film density.

X-Ray Reflectivity (XRR) numbers among the most conventional methods of thin film characterization; nevertheless, it is able to overcome most of these difficulties. XRR is a non destructive and fast technique with an angström resolution. It probes on a large surface area. The variation of the electron density of complex film stacks in the μm-nm thickness range, and it is still pertinent for layers of just some atomic layers.[21] The so-called Kiessig fringes, obtained in XRR data, arise from the interference between the waves backscattered by the different layers. Their positions and intensities inform on the thicknesses, roughnesses, and densities of these layers. On the other hand, x-ray absorption spectroscopy is a powerful technique to get information on the local chemical and structural environment of selected chemical species. The analysis of the lower energy range of the absorption spectra, a technique called X-ray Absorption Near Edge Spectroscopy (XANES), is more specifically sensitive to the symmetry and the three-dimensional organization around the absorbing atoms. Coupling XRR and XANES may substantially improve the characterization of fabrication process of magnetic nanostructures.[22]

In the Pt/Co/AlO_x systems of our interest, a previous study has shown a change of the magnetic anisotropy from

---

a)Author to whom correspondence should be addressed. Université de Djibouti, Avenue Georges Clemenceau BP 1904 Dijibouti.

in-plane to out of plane with oxidation and/or annealing.[23] It has been guessed that this change was related to the diffusion of the oxygen toward the Co/AlO$_x$ interface. The Co-Al bonds would then be replaced by Co-O ones, all these phenomena depending on the annealing temperature (T_{Ann}) and on the oxidation time (t_{Ox}). The structural characterization of these trilayers has been investigated by XPS[24] in the as-deposited system. Recently, preliminary XRR results have confirmed the formation of CoO and AlO$_x$ phases by varying both t_{Ox} and T_{Ann} for some isolated trilayers.[25,26]

However, the origin of Perpendicular Magnetic Anisotropy (PMA) is not clear: Is there oxygen at the interfaces between Co and AlO$_x$? Is there a CoPt intermixing caused by the annealing? Are there chemical modifications? Does the roughness play a role on PMA? The main focus of the present paper is to contrast the possible models at the origin of the improved perpendicular magnetic anisotropy. The structural evolution as a function of t_{Ox} and T_{Ann} is investigated by XRR and XANES for a complete series of samples. We establish the different structural schemes indicating the nature of present phases (either Pt or CoPt, either Co or CoO, either Al or AlO$_x$), as well as the topology and density of the layers. The combination of the two techniques unambiguously shows the competition between CoO and CoPt phases alloys as a function of the quantity of oxygen (favoring CoO) and the annealing process (favoring CoPt), providing a clear understanding of evolution of the magnetic properties at room temperature[23] in the Pt/Co/AlO$_x$ system.

This paper is organized as follows: Section II describes the XRR and XANES experiments. Section III A is devoted to the reflectivity results performed on a series of samples corresponding to different magnetic states. The results of the local analysis performed by XANES are presented in Sec. III B. Finally, a complete description of the structural schemes governing the macroscopic properties is given in Sec. IV. The magnetization results measured at room temperature[23] are discussed in the light of these outcomes.

II. EXPERIMENT

The Si/SiO$_2$/Pt(3 nm)/Co(0.6 nm)/Al(1.6 nm) multilayers were dc-magnetron sputtered following a procedure described in Ref. 23. They were then transferred under vacuum in a separate treatment chamber and oxidized using an oxygen rf plasma (partial pressure of 3.0×10^{-3} mbar, power of 10 W). Different oxidation times ranged from 15 to 60 s by steps of 5 s. Annealing was performed *ex situ* in a high-vacuum furnace during 30 min. Different temperatures T_{Ann} were used from room temperature up to 450 °C by step of 50 °C. In the following, $T_{Ann} = 20$ °C corresponds to the as-deposited sample.

The reflectivity measurements were carried out with a Bruker D8 Discover diffractometer using a line focus from a Cu target x-ray tube. Göbel multilayer optics was used to select Cu wavelength ($\lambda = 0.15418$ nm) and to make the beam quasi-parallel (divergence $\leq 0.028°$). The beam size at sample position was 50 μm. The sample size was 3 mm wide by 12 mm long. Data were collected using a scintillation detector in the [0–16°] 2θ angular range, with an increment of

0.02° and an acquisition time of 40 s/step. The forward diffuse scattering measured in an offset θ–2θ scan was subtracted from the specular scattering. The XRR curves are expressed as a function of the momentum transfer Q_Z ($=[4\pi/\lambda] \sin\theta$). The analysis of XRR measurements is carried out by fitting the experimental scans with theoretical curves using the Bruker LEPTOS software.[27] The calculation procedure is based on a recursion formula first announced by Parrat.[28] The parameters extracted from these adjustments are the layer thickness, the layer density, and the interface roughness, for each layer constituting the system.

The XANES measurements were carried out at the French CRG BM30B beamline at ESRF (Grenoble, France), and at the KMC2 beamline at BESSY II (Berlin, Germany). In order to study the linear dichroism in the XANES spectra, the samples were mounted on a precision gionometer. For in plane measurements, the polarization vector, namely ϵ, was at 10° from the film surface. In this geometry, principal contribution comes from the atomic bonds in the plane of the film. For out of plane measurements, ϵ was at 10° from the normal to the film. Gas ionization chambers were used to measure the incoming beam. Fluorescence signals were detected using a Canberra 30 element solid state detector. Bulk Co and CoO references were measured in the same conditions. After background subtraction of the absorption spectra by linear extrapolation below the pre-edge region, the spectra were normalized in the range of (7700–8000) eV.

III. STRUCTURAL CHARACTERIZATIONS

A. x-ray reflectivity measurements

The results are presented for samples where annealing temperatures are fixed. Fig. 1 displays x-ray reflectivity data for Pt/Co/AlO$_x$, for the as deposited trilayer [(a)], and for the same trilayer annealed, at different temperatures $T_{Ann} = (200$ [(b)], 300 [(c)], and 450 °C [(d)]), and oxidized with different values of $t_{Ox} = (15$-25–40-55) s. The Kiessig fringes are weakly apparent for the as-deposited [Fig. 1(a)] and low annealing temperature [200 °C, Fig. 1(b)] samples. For $T_{Ann} = 450$ °C [Fig. 1(d)], the XRR data seem to be insensitive to t_{Ox}. For the other annealed multilayers, higher is t_{Ox}, more the x-ray reflectivity peaks appear narrow and marked, revealing a modification of the layer composition. Moreover, the oxidation time induces a displacement of the position of the Kiessig fringes, at least for the moderate annealing temperatures, as indicated by the arrows in Fig. 1. Higher is T_{Ann}, less dependent on t_{Ox} are the shifts and sharpening of the Kiessig fringes. A probable explanation is the reduction of the thicknesses of metallic layers (Co and Al) for the benefit of CoO and AlO$_x$ layers, due to the oxidation process.

In order to fit the XRR curve, and to extract structural information, models of stacks have to be defined. The lowest oxidized ($t_{Ox} = 15$ s) and as-deposited trilayer is chosen as the first studied sample, because we can safely guess that only the top layer (Al) is partially oxidized, and the oxygen atoms penetrate slightly into the buried layers. The architecture of this initial multilayer is then Pt/Co/Al/AlO$_x$ with Pt and Co thicknesses close to nominal values. With the best set of parameters obtained for this sample as starting values,
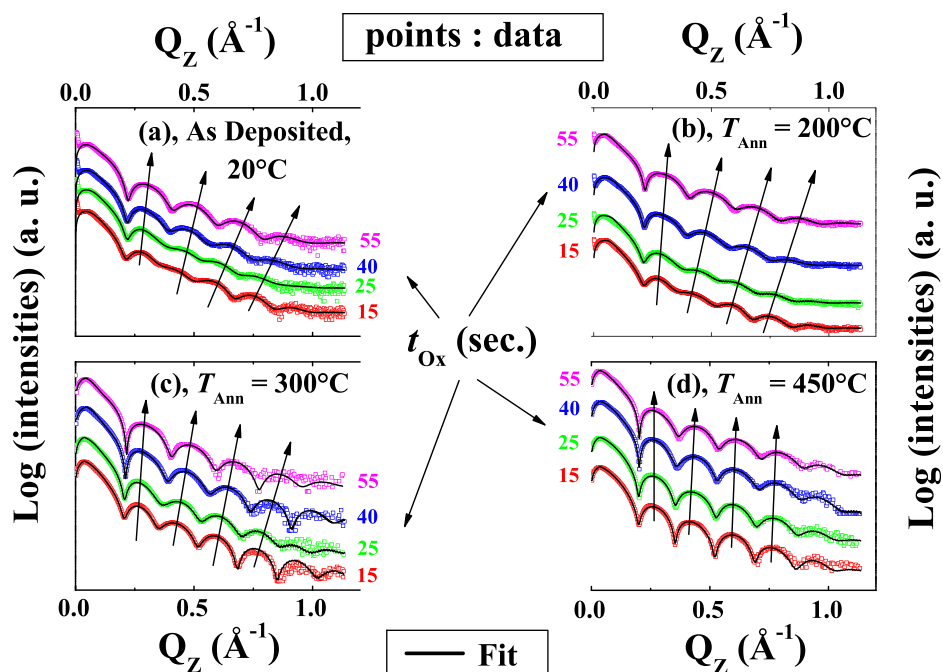
FIG. 1. x-ray reflectivity data (points) with fittings (solid lines) for Si/SiO$_2$/Pt(3 nm)/Co(0.6 nm)/AlO$_x$(2 nm) oxidized during t_{Ox} = (15-25-40-55 s), as-deposited or T_{Ann} = 20 °C [(a)] and annealed at T_{Ann} = (200 [(b)], 300 [(c)], and 450 °C [(d)]). The curves are shifted vertically for the sake of clarity.

subsequent oxidized sample data are adjusted with the same stack (Pt/Co/Al/AlO$_x$). The procedure is iteratively repeated for the as-deposited sample series [see Fig. 1(a)]. Due to the large number of parameters in the model, density and thickness of Co and Pt layers were fixed to nominal values at the beginning of the simulation, and released only for the final fitting. We should consider the partial oxidation of the Co layer, i.e., the stack Pt/Co/CoO/AlO$_x$. This occurs for oxidation times higher than a certain value, namely t_{Ox}^*, different for each annealing temperature. Finally, for the highest annealing temperature (T_{Ann} = 450 °C), the possibility that a Pt-Co alloy might be fabricated during the annealing process, should be taken into account, as in Refs. 29 and 30. Consequently, a third stacking Pt/Co-Pt/AlO$_x$ is proposed in the fitting procedure for the 450 °C annealed samples. Only a

fraction of the Pt layer (3 nm) is alloyed with the very thin Co layer (0.6 nm). The fitting of the data gives for the resulting Pt buffer layer following values close to: thickness ≈2.87 nm, roughness ≈ 0.41 nm, and density ≈20.48 g/cm^3.

For each XRR curve in Fig. 1, three parameters are extracted for each layer of the architecture: the thickness (Th), the roughness rms (σ), and the density (ρ). The variations of thicknesses Th with the annealing temperature T_{Ann} are displayed in Fig. 2 for samples oxidized during t_{Ox} in the (15-55) s range for AlO$_x$ [(a)], CoO [(b)], Al [(c)], and Co or CoPt [(d)]. Whatever is the oxidation time, the oxidized and metallic parts are inverted for the (Al,AlO$_x$) and (Co,CoO) couples when T_{Ann} is increased, as expected. The presented results in Fig. 2 are detailed in the following paragraphs by separating low and high t_{Ox} values.
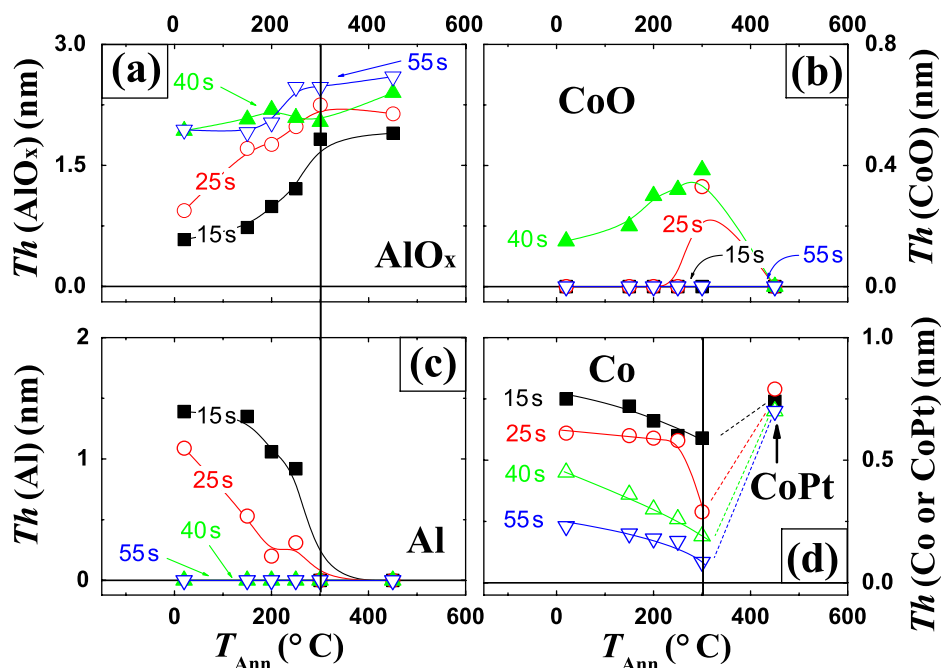

FIG. 2. Thermal annealing (T_{Ann}) dependence of thicknesses Th for Pt/Co/AlO$_x$ samples oxidized during t_{Ox} for the following layers: AlO$_x$ [top-left panel (a)], CoO [top-right panel (b)], Al [bottom-left panel (c)], and Co (for T_{Ann} ≤ 300 °C) or CoPt alloy (for T_{Ann} = 450 °C) [bottom-right panel (d)].

(1) For small t_{Ox} (15–25 s), the decrease of Th(Al) [Fig. 2(c)] is accompanied by an increase of Th(AlO$_x$) [Fig. 2(a)] for increasing T_{Ann} with comparable slopes of Th with T_{Ann} (with opposed signs). A weak decrease of Th(Co) with T_{Ann} is also observed, and Th(CoO) ≈ 0 (no CoO layer detected), except for the sample oxidized for $t_{Ox} = 25$ s and annealed at $T_{Ann} = 300\,°C$. This is due the fact that the Al layer is oxidized before the Co one. Starting from $T_{Ann} = 300\,°C$ (see the vertical line in Figs. 2(a) and 2(c)), the AlO$_x$ layer is fully oxidized (Th(Al) ≈ 0). At the same time, the CoO layer seems to be absent, and a CoPt alloy appears for the highest annealing temperature value (450 °C). To summarize, for such moderate oxidation times (15–25 s), a change from a mixed phase of [Al and AlO$_x$] to a pure AlO$_x$ is observed when T_{Ann} increases in the (20–300) °C range, followed at $T_{Ann} = 300\,°C$ by a change from a mixture of Co and CoO layers to a CoPt one for larger T_{Ann} (450 °C).

(2) For high t_{Ox} (40–55 s), no Al layer is detected, whereas a stabilization of AlO$_x$ thickness appears for any annealing temperatures. At the same time, a coexistence of Co and CoO layers persists for moderate T_{Ann} (300 °C). The oxidation front reaches the Co layer even without annealing, inducing a CoO phase. Once again, a unique CoPt layer is suspected for the largest T_{Ann} value (450 °C) whatever t_{Ox}.

The most important points appearing in Fig. 2 are the remarkably weak dispersion of (i) Th(AlO$_x$) (2.1 nm) for the high t_{Ox} regime (40–55 s) with no Al layer; (ii) Th(AlO$_x$) (2.1 nm) and CoPt (0.7 nm) for the highest T_{Ann} value (450 °C) and whatever t_{Ox}, with no residual Al and Co layers. In the same way, for such over oxidized trilayer, the density (second parameter deduced from fittings of XRR data) of AlO$_x$ reaches the same bulk value [ρ(AlO$_x$) = 3.98 g/cm^3] for any T_{Ann} value, as represented in Fig. 3(a). At fixed T_{Ann}, the higher t_{Ox} is, the more ρ(AlO$_x$) is [see the top part in Fig. 3(a)]. The ρ densities for Co and Al are weakly dependent with T_{Ann} [Figs. 3(a) and 3(b), respectively]. A noteworthy result is the strong value of ρ(Co) for $t_{Ox} = 40$ s, which is close to expected bulk value (8.9 g/cm^3) for any T_{Ann} (as well as for the alumina layer). An additional remark concerns the weakness of ρ(CoO) compared to the bulk value (6.43 g/cm^3) due to the inhomogeneity of the oxidation front, which causes a non dense CoO layer (because Al oxidizes before Co). These results concerning the density of AlO$_x$, which increases with both t_{Ox} and T_{Ann}, indicate the progressive formation of the alumina layer with the oxidation time and the annealing temperature, as observed from the dependencies of Th(AlO$_x$) with t_{Ox} and T_{Ann} [Fig. 2(a)]. A second relevant result is the remarkable densities of Co and AlO$_x$ for $t_{Ox} = 40$ s and $T_{Ann} = 300\,°C$. An increase of both the thickness and the density with the oxygen plasma time for an Al$_2$O$_3$ top layer has been observed by Quade *et al.*[31] for Si/Al$_2$O$_3$(1 nm)/Al(32–59 nm)/Al$_2$O$_3$(2 nm) multilayer. Moreover, an increase in the density of the alumina Al$_2$O$_3$(40 nm) is deduced from XRR analysis, when Al$_2$O$_3$/SiC structures are exposed to annealing (20–1000 °C),[32] as for our present study.
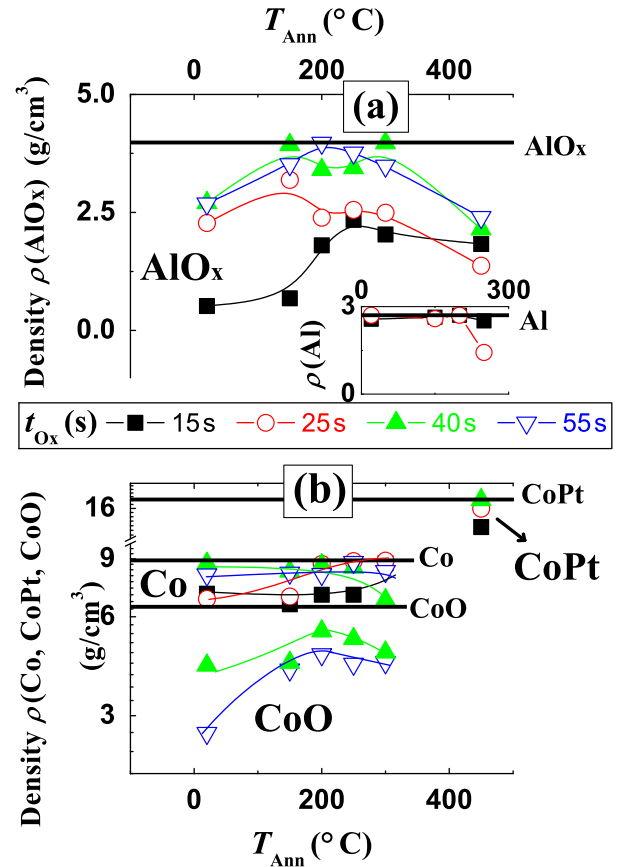

FIG. 3. Thermal annealing (T_{Ann}) dependence of densities (ρ) for Pt/Co/AlO$_x$ samples oxidized during t_{Ox} in the range (15-25-40-55) s for the following layers: AlO$_x$ (top part) and Al (inset) [top panel (a)], Co or CoPt alloy (top part), and CoO (bottom part) [bottom panel (b)]. Bulk values are added in straight lines.

At this point, it appears to be interesting to combine Th and ρ, extracted from fitted XRR curves, for a given layer. The following ratios are defined:

$$R(Al) = \frac{\rho(Al) \cdot Th(Al)}{\rho(Al) \cdot Th(Al) + \rho(AlO_x) \cdot Th(AlO_x)}, \quad (1)$$

$$R(AlO_x) = 1 - R(Al). \quad (2)$$

R(Co) and R(CoO) are defined in a similar way. The evolutions of R(AlO$_x$) and R(Co) with t_{Ox} for different annealing temperatures T_{Ann} are shown in Fig. 4. We note that t_{Ox}^* is diminishing when T_{Ann} is increasing (see the vertical arrows). The crossover oxidation times t_{Ox}^* are merged in Table I. At this step, one neglects the roughness, and only the ratio R is used to optimize the deposition parameters. A maximization of both ρ(AlO$_x$/Co) and Th(AlO$_x$/Co) associated to a minimization of both ρ(Al/CoO) and Th(Al/CoO) can be chosen from Figs. 4(a) and 4(b) as a function of t_{Ox}^* and T_{Ann}. This is merged in Table I, where the optimization of semi-tunnel junction is found according to the t_{Ox}^* and T_{Ann} values.

When including the roughnesses of layers in the fitting, one gets values close to a fraction of thickness of the corresponding layers [Figs. 4(c) and 4(d)]. For instance, for $t_{Ox} = 35$ s and $T_{Ann} = 150\,°C$, the roughness reaches 53% and
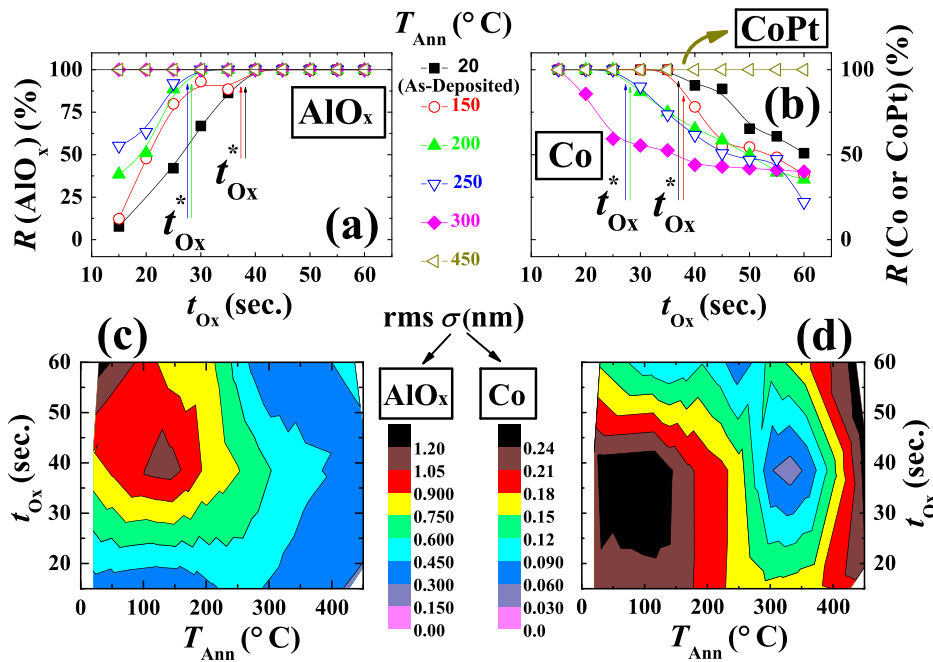
FIG. 4. Ratios of the thicknesses of AlO_x, $R(AlO_x)$ [top-left panel (a)] and Co, $R(Co)$ [top-right panel (b)], calculated starting from parameters deduced from fittings of Fig. 1, as a function of both the oxidation time t_{Ox} and the annealing temperature T_{Ann} for Pt/Co/AlO_x samples. t_{Ox} and T_{Ann} are varied in the (15–60) s and (20–450) °C ranges, respectively. The vertical arrow is the oxidation time t_{Ox}^* starting from the Al layer is fully oxidized, whereas a CoO layer appears. Map of the roughness rms σ of AlO_x, $\sigma(AlO_x)$ [bottom-left panel (c)] and Co, $\sigma(Co$ or $CoPt)$ [bottom-right panel (d)] for such samples, the scale being in nm. The lowest value of T_{Ann} (20 °C) corresponds to the as-deposited sample.

52% of thicknesses of Co and AlO_x, respectively. For appropriate values of t_{Ox}^* and T_{Ann}, the roughnesses of cobalt and alumina layers can be reduced (Table I). For the low T_{Ann} regime, a maximum for $\sigma(AlO_x)$ and a lowering of $\sigma(Co)$ take place when t_{Ox} is increasing. During oxidation of the trilayer, at moderate T_{Ann}, the roughness of the top layer is increased. The values of σ are constant whatever t_{Ox} for $T_{Ann} \approx 400$–450 °C. Typical values of thicknesses Th and roughnesses σ are given for $t_{Ox} = t_{Ox}^*$ in Table I. By increasing T_{Ann}, the σ/Th ratio is lowered, meaning a lowering of the roughness and a preservation of the thickness. One obtains thus a smoothing of the layers with the annealing. Raju *et al.*[33] have obtained a similar result (reduction of the rms-roughness by increasing the growth temperature in the 75–250 °C range) at the interface between CoFe and MgO, using a combination of specular and diffuse XRR measurements. A sharpening of the interface between CoFeB (3 nm) and AlO_x(1.2 nm) layers during *in situ* annealing (20–400 °C) was also observed using high-resolution grazing incidence x-ray scattering experiments by Pym *et al.*[34]

Systematic XRR studies on magnetic nanostructures combining ferromagnetic and oxidized layers, when both the oxidation time and the annealing temperature are varied for different series of samples, are surprisingly scarce in the literature. Only XRR studies for some as-deposited samples (not a complete series) with different oxidation times,[35–37] and for some annealed ones (not a complete series) with a fixed oxidation time,[38] are reported. In the present paper, the series of samples are very complete, providing a safe evaluation of the T_{Ann} and t_{Ox} parameters for improving the structural quality of the present system. Notable densities for Co (6.75 g/cm^3) and AlO_x (3.97 g/cm^3), high thickness for AlO_x, associated to a preserved Co thickness, and lowered roughnesses for Co and AlO_x are obtained for a particular trilayer ($T_{Ann} \approx 300$ °C and $t_{Ox} \approx 40$ s, last line of Table I). A main result is the fact that fits' parameters tend to comparable values after high annealing (450 °C) whatever the oxidation time. This is probably due to the formation of a thin Co-Pt layer, as confirmed by the next section.

B. XANES measurements

Fig. 5 displays the Co-K XANES spectra of the as-deposited series of trilayers as a function of t_{Ox}. The structures corresponding to the bulk Co and bulk CoO are partially visible in the trilayer samples. One notes the pre-edge feature (A) at 7712.1 eV corresponding to Co and the white line (B) at 7726.4 eV for CoO. A third peak (C) at 7753.3 eV appears between the ones expected for CoO and Co, respectively, at 7741.5 eV (peak named 2) and 7759.2 eV (peak named 3). These latter peaks, as well as the Co one at 7733.8 eV (peak named 1) are absent in the as-deposited trilayer spectra. These curves seem to be some interpolation between the spectra of the reference samples, Co and CoO.[39] When t_{Ox} increases, the pre-edge (A) decreases and the white line becomes higher. At the same time, the peak (C) decreases and the rest of the spectra tends to a plateau. The persistent differences between the references and the samples are mainly due to the thinness of the deposited Co layers (0.6 nm) of the same order than the mean free path of the photoelectron. It also comes from additional contributions

TABLE I. Crossover t_{Ox}^* value (starting from a fully oxidized Al layer is obtained), thickness Th, and roughness σ for Co, CoPt, and AlO_x layers as a function of T_{Ann} deduced from fits' parameters coming from adjustments of reflectivity data. CoPt is uniquely obtained for $T_{Ann} = 450$ °C. Additional results are given for the sample elaborated for $t_{Ox} = 40$ s and annealed at $T_{Ann} = 300$ °C.

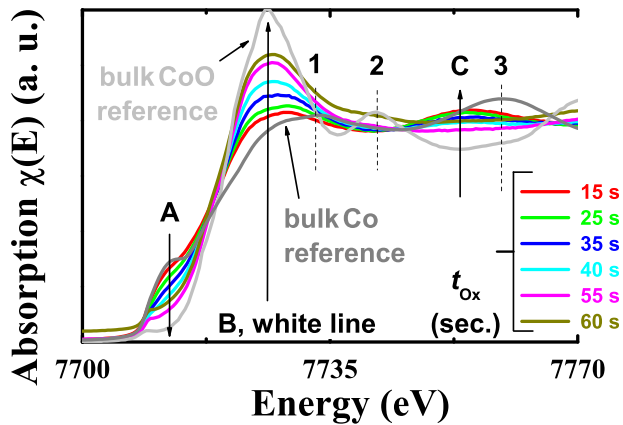| T_{Ann} (°C)	t_{Ox}^* (s)	Th(Co or CoPt/AlO_x) (nm)	σ(Co or CoPt/AlO_x) (nm)
20–150	40	0.45–0.36/1.93–2.07	0.23–0.20/0.82–1.20
200–250	30	0.45–0.40/2.14–2.17	0.24–0.21/0.98–0.73
300–450	15	0.59–0.74/1.8–1.9	0.16–0.21/0.26–0.44
300	$t_{Ox} = 40$ s	0.19/2.04	0.06/0.65

FIG. 5. Co-K edge XANES normalized profiles for as-deposited Pt/Co/AlO$_x$ trilayers and oxidized for different oxidation time t_{Ox}. Note the evolutions of typical peaks [A (pre-edge), B (white line), and C] as a function of t_{Ox}. Bulk references for Co and CoO are added for comparison. The 60 s is slightly shifted towards positive absorption for clarity of presentation (very close to the 55 s line).

(as Co-Pt bonds, for instance) not taken into account at this point, but discussed below.

An estimate of the relative Co and CoO contributions can be deduced from the surface under the white line. On the left part of Fig. 6 is plotted the evolution of this surface under the white line as a function of t_{Ox}. This corresponds to the integral over energy of the spectra, in the interval [E$_{min}$,E$_{max}$] (see the square symbols), starting from the edge step χ_{min} (see the inset in the figure). The plotted values are relative to the CoO compound arbitrary set to 100%. For example, for $t_{Ox} = 40$ s, the white line area reaches 50% of the CoO ones. From this, one gets that the percentage of CoO and Co in the sample is close to 50%. A linear behavior of the integral is observed indicating a progressive oxidation of the Co layer from 18% up to 76% when the oxidation time increases in the (15–60) s range. By extrapolating this linear behavior, a full oxidation of Co might be obtained for $t_{Ox}^{full} = 83$ s.

To support this phenomenological analysis, we resort to *ab initio* simulations. We used the FDMNES code,[40] in its

multiple scattering framework which employs the muffin-tin approximation on the shape of the potential. To simulate the inhomogeneous Co layer, different structures and compositions were tested. The first one is a simple layer composed of two Co planes. For the second one relating to CoO, different local geometries (octahedral and tetrahedral form) are considered. To minimize the disorder, we used different cluster radius around the absorbing energy. Usual simulations in bulk material need cluster radius up to typically 0.6 or 0.7 nm. We found that better agreement is obtained with a radius corresponding to only one shell around the absorbing atom. Moreover, the best agreement is found with Co atoms in a tetrahedral environment, and with a 0.20 nm Co-O bond length. This value is slightly higher than the one found for the tetrahedral Co site in Co$_3$O$_4$. The two models were then summed up with weights corresponding to their supposed proportions in the layer. For the as-deposited sample, we found a very good agreement between the data and the simulations (Fig. 7). We thus confirm the progressive oxidation of the Co layer with remarkable agreements on the oxide proportion, as seen in Fig. 6 (left and right parts).

To compare the data [Figs. 8(a)–8(d)] and the simulations [Fig. 8(e)] for different oxidation times and different annealing temperatures, some fractions of CoPt are included in the FDMNES code. The calculated spectra are given for the pure
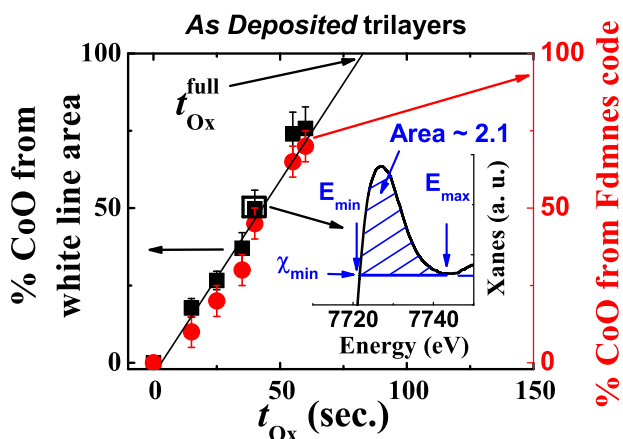

FIG. 6. Normalized white line area (left), corresponding to the normalized peak B appearing in Fig. 5, and content of CoO deduced from *ab initio* simulations[40] (right) versus t_{Ox} for as-deposited Pt/Co/AlO$_x$ trilayers. Inset: Example of integration of the white line (normalized intensity) for $t_{Ox} = 40$ s with the values for the energy (E$_{min}$ and E$_{max}$) and the minimal XANES normalized intensity (χ_{min}) used for calculating the areas.
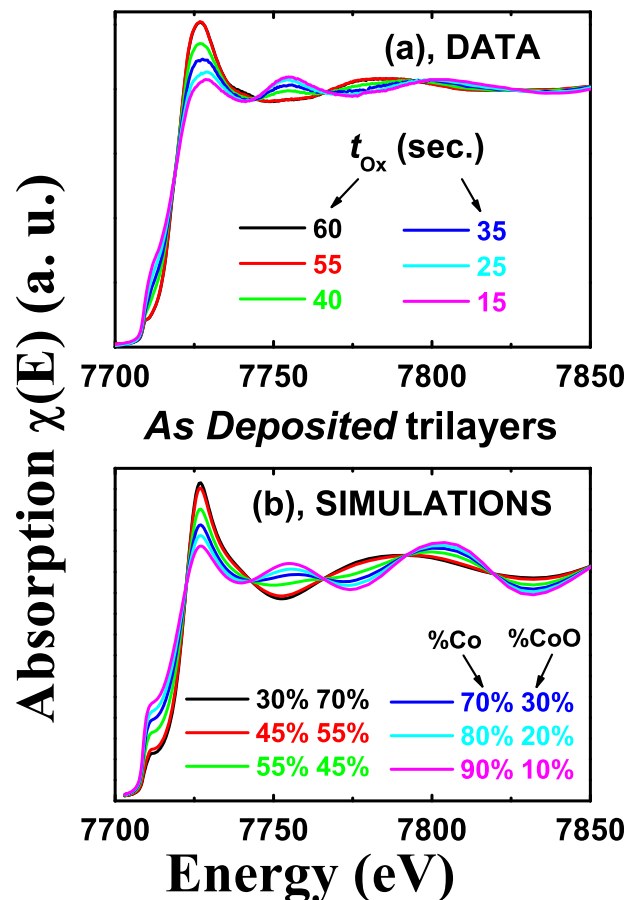

FIG. 7. Experimental (a) and simulated (b) Co-K edge XANES data for as-deposited Pt/Co/AlO$_x$ trilayers as a function of the oxidation time t_{Ox}. Here, data are fitted with the help of FDMNES code[40] starting from a linear combination of calculated spectra for Co and CoO$_x$.
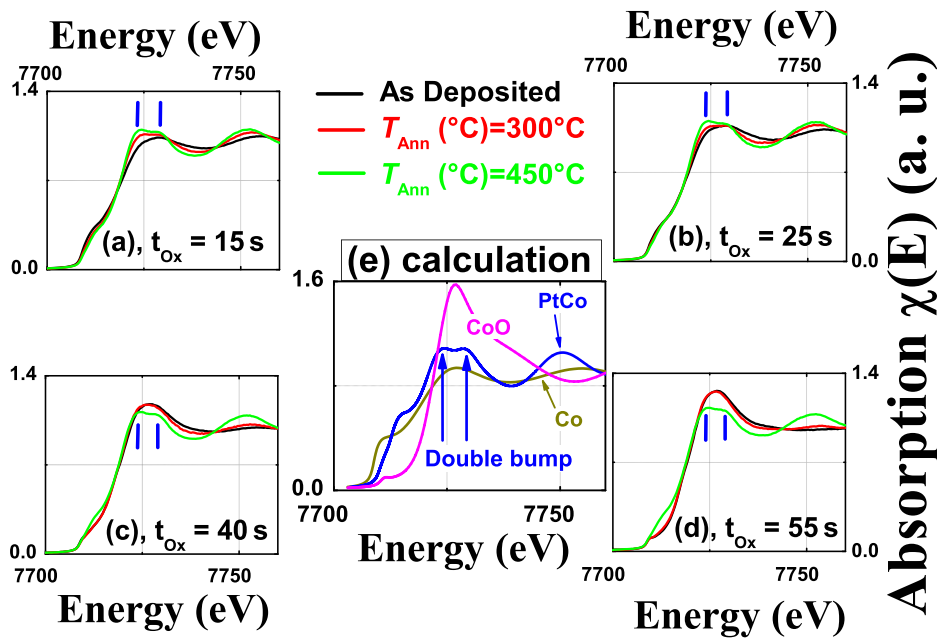
FIG. 8. Experimental (a)–(d) and simulated (e) Co-K edge XANES data for as-deposited $Pt/Co/AlO_x$ trilayers oxidized during different oxidation times t_{Ox} [(a) 15 s; (b) 25 s; (c) 40 s; (d) 55 s], and annealed for different temperatures T_{Ann} (300 °C and 450 °C).

Co, CoO, and CoPt phases. For the simulation of CoPt, the best agreement is reached with rather high cluster radius: 0.55 nm. This corresponds to 25 atoms in the sphere of calculation. Because of this bigger radius, and to be closer to the thin layer description, we also used inside the sphere a slab, not the 3D alloy. To build this slab, we started from the face centered cubic structure with 0.383 nm lattice parameter, but with a 25% of Pt is this alloy (corresponding to Co_3Pt phase). In accordance with the XRR fitting, XANES simulations indicate that the Pt layer is partially alloyed with Co for samples annealed at 450 °C. Simulations using the $L1_0$ structure lead to a lower agreement. The higher value of the radius suggests a good crystallinity of the layer after annealing. Similar XANES calculation from a full-potential linearized-augmented-plane-wave method is found in Ref. 41. For small oxidation times (15 and 25 s), as soon as T_{Ann} reaches 300 °C, the XANES profile shows a small flat shape just after the rising edge,

indicating a change in the environment of the Co atoms. For $T_{Ann} = 450$ °C, we see at the same energy the formation of a double bump equivalent to the ones observed in CoPt. The energy difference ($\cong 3.6$ eV) between these 2 bumps is slightly smaller than the 4.2 eV observed in pure CoPt. For these 450 °C annealed samples, the content of oxygen is small, thus the Co-Co and Co-Al bonds might be replaced principally by CoPt bonds. For higher oxidation times (40–55 s), one needs annealing up to $T_{Ann} = 450$ °C to see the appearance of the double bump, with a lower energy difference ($\cong 3.2$ eV) between them. For such oxidized samples, Co-O bonds are not negligible compared to Co-Co bonds. Only a strong annealing temperature leads to mix cobalt and platinum, as if the presence of Co-O bonds rigidifies the Pt/Co interface, and avoids its intermixing, point already assumed by Rodmacq *et al.*[23]

Now, let us analyze the linear dichroism of the as-deposited sample weakly oxidized [$t_{Ox} = 15$ s, Fig. 9(a)] and

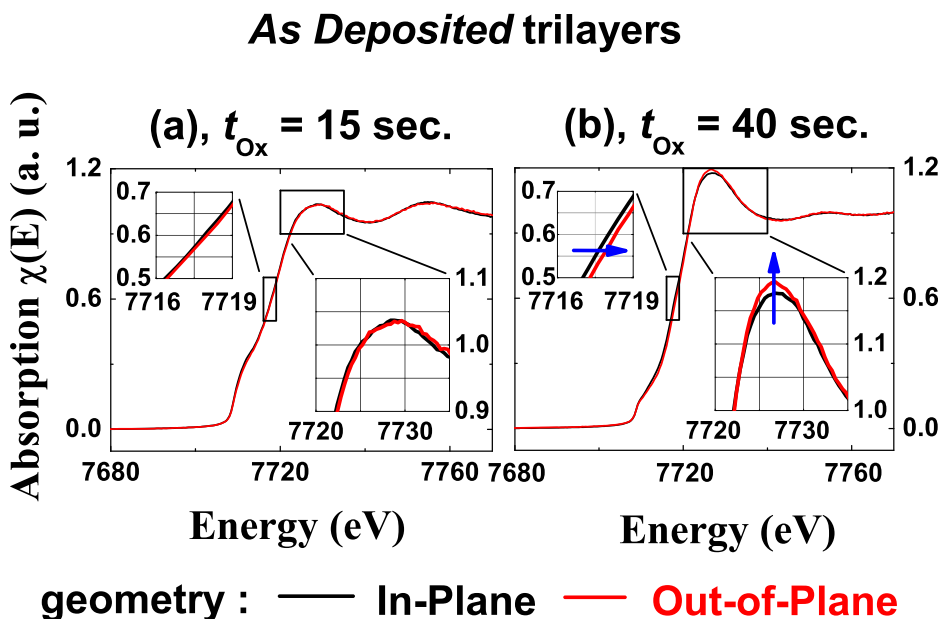## *As Deposited* trilayers

FIG. 9. Co-K edge XANES normalized profiles for as-deposited $Pt/Co/AlO_x$ trilayers, for in-plane and out-of-plane polarization geometries, and oxidized for $t_{Ox} = 15$ s [(a)] and 40 s [(b)]. Insets: Zoom of the Co-K edges. Note the differences for only $t_{Ox} = 40$ s, where the Co-oxygen bonds are reinforced for the out-of-plane configuration (see the arrows).
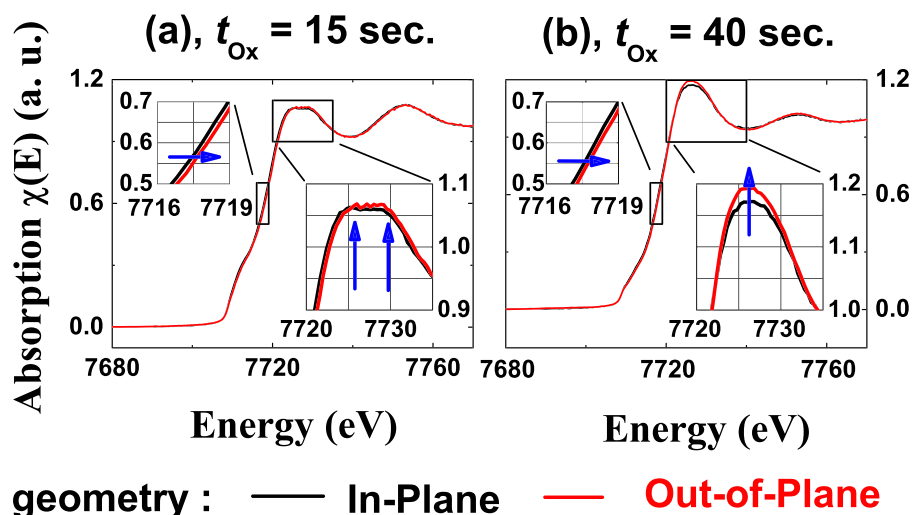
FIG. 10. Co-K edge XANES normalized profiles for annealed Pt/Co/AlO$_x$ trilayers at $T_{Ann} = 300\,°C$, for in-plane and out-of-plane polarization geometries, and oxidized for $t_{Ox} = 15\,s$ [(a)] and 40 s [(b)]. Insets: Zoom above the Co-K edges. Differences appear for $t_{Ox} = 40\,s$: the contribution of Co-oxygen bonds is stronger for the out-of-plane configuration (see the arrows).

highly oxidized [$t_{Ox} = 40\,s$, Fig. 9(b)]. There is nearly no difference between the in plane and out of plane measurements for the lowest oxidation time. On the contrary, a clear difference appears with $t_{Ox} = 40\,s$. In the out of plane polarization geometry, the edge is shifted towards higher energy and the white line is slightly increased, its integral reaching 50%, in place of 50% for the in plane situation. The shift of the absorption edge to higher energies indicates an increase of the overall oxidation state,[42] or a modification of the interatomic bondings. Isotropic signal is a signature of cubic or disordonned geometries. Anisotropy comes from a decrease of the symmetry connected to an interface effect. At the K edge, when the polarization is out of plane, the photoelectron probes $4p_z$ Co orbital perpendicular to the barrier. On the contrary, when the polarization is parallel to the interface, the $4p_x$ and $4p_y$ levels are probed, these last been part of intra-layer bonds. The most probable situation to get an increase of the white line and a displacement when polarization is out of plane is thus the of Co-oxygen bonds at the interface between Al and Co than in the Co layer itself.

The samples annealed at $T_{Ann} = 300\,°C$ exhibit a shift of the edge and a modification of the white line for both oxidation times, 15 s and 40 s (see Fig. 10). The effect is stronger for the higher oxidation time. A competition appears between Co-oxygen bonds induced by the oxidation process (driven by t_{Ox}) and the formation of CoPt alloy induced by the annealing (driven by T_{Ann}). Higher is the oxidation time, lower is the CoPt formation.

IV. DISCUSSION

XRR and XANES show that the existence of Co, CoO$_x$, and CoPt$_x$ is strongly dependent on both t_{Ox} and T_{Ann}. Both techniques give the same trend for the variation of the Co-O bonds versus t_{Ox}. But certain differences can be outlined by comparing Figs. 4(b) and 6. A XRR layer by layer analysis is less adapted for such a thin slab containing moreover intermixing. XANES on the contrary is a local probe, which sounds directly the different bonds, and thus, as XPS,[24]

XANES keeps its sensitivity for very thin layer study.[47] Moreover, the local geometry, tetrahedral rather than octahedral, as well as Co$_3$Pt rather than CoPt, is found from XANES simulations. On the other side, density and roughness of each layer are determined uniquely by reflectometry adjustments, revealing the intermixing between layers and its porosity. Finally note that, by supposing a wrong stack, as for instance a Co layer rather than a CoPt one, in the case of annealed samples, would give a satisfying but erroneous XRR data adjustment. This indicates that we have to be prudent with XRR analysis alone.

The annealing process induces a residual bottom Pt layer and a top Co$_3$Pt alloy from both techniques (XANES and XRR). This is understood by the low Co thickness (0.6 nm) compared to the Pt one (3 nm). In the literature, intermixing analysis due to annealing process using XRR has already been reported for complex structures. Gonzalez-Silveira *et al.*[43] have observed the occurrence of CuMg$_2$ alloy in a Cu/Mg/Cu/Fe multilayer after an annealing process, by considering the phase diagram of the studied compound. Other examples of intermixing have already been observed using complementary techniques. It is the case, for instance, for Al-Cu with the help of x-ray photoemission, EXAFS, and Rutherford Backscattering Spectrometry,[44] or in HfO$_2$-Al$_2$O$_3$ by the mean of high angle x-ray diffraction measurements.[45] XANES shows better how the Co$_3$Pt alloy takes gradually place when increasing the annealing temperature. The appearance of Co$_3$Pt is more abrupt in the XRR study, where CoPt is observed only at 450 °C. In fact, the definition of the multilayer is essential for proper XRR simulations. Combination of both techniques,[46] XRR and absorption spectroscopy, permits a safer conclusion concerning the nature of the multilayer. In our system, competitions between Co-oxygen and Co-platinum are roughly given as a function of t_{Ox} and T_{Ann} by both techniques. This competition between both phases is coherent with the values of enthalpy of formation $(-\Delta H_f)$ of these oxides. $-\Delta H_f$ reaches 137.7 kJ/atom and 6.5 kJ/atom for CoO and Co$_3$Pt, respectively (452.5 kJ/atom for AlO$_x$).[47] This explains why CoO is

induced for as-grown samples, and that annealing favors the appearance of Co_3Pt.

Now, we discuss the room temperature magnetic properties of the system at the light of our structural results:[23,26]

(i)   For as-deposited samples and increasing t_{Ox}, a crossover between $Pt/Co/Al/AlO_x$ and $Pt/Co\text{-}CoO_x/AlO_x$ stacks is observed. In particular, $t^*_{Ox} = 40\,s$ appears to be a reasonable oxidation time for obtaining a high-quality AlO_x layer (both maximized Th and ρ), but with marked roughnesses for the different layers. Thus, inhomogeneous oxidation must be due to inappropriate deposition parameters (plasma pressure and power). By increasing t_{Ox}, Co-Al bonds are replaced by Co-O ones. This favors the appearance of an out-of-plane anisotropy for $t_{Ox} > 25\,s$, and a maximum of anisotropy field for $t_{Ox} \approx 35 - 40\,s$,[23] precisely for the optimized sample as deduced from the XRR analysis. The influence of a ferromagnetic/antiferromagnetic (Co-CoO_x) coupling is also observed in the low temperature regime of magnetic properties.[26,48] In addition, Rodmacq *et al.*[23] found that the amplitude of the Hall resistance considerably decreases for the longest oxidation times.[23] We show here that it is explained by the appearance of CoO_x. Moreover, the multi-domain structures,[23] at the origin of the magnetic loop at room temperature for samples oxidized during $t_{Ox} > 40\,s$, come from the insertion of oxygen in the cobalt layer.

(ii)   By increasing T_{Ann} up to $300\,°C$, both AlO_x and Co layers exhibit remarkable morphological and chemical qualities: preserved thicknesses, diminished roughnesses, and marked densities. There appears a competition between CoO_x and CoPt coming from the oxidation and annealing process, respectively, and leading to a partial deoxidation of CoO_x. Nevertheless, the thermal annealing is not sufficient to get for a complete CoPt formation. Thus, a $Pt/Co/CoO_x/AlO_x$ (with residual Al atoms) might be assumed where a densification, a smoothing, and an improvement of the thickness of the alumina layer, as well as the cobalt one, are obtained. An homogeneous alumina layer is elaborated even for low oxidation time ($t_{Ox} \approx 15\,s$) for the stack annealed at $T_{Ann} \approx 300\,°C$ as found from the reflectometry measurements [Fig. 4(b)]. As a result, remarkable magnetic properties might be measured for such values of annealing temperatures and appropriate oxidation time. Indeed, the PMA reaches a maximum for annealing temperatures close to $300\,°C$ and oxidation times reaching $35-40\,s$.[23] Such deposition parameters permit to improve the structural and chemical qualities of the multilayer. Thus, the annealing homogenizes the barrier and improves the Co/AlO_x interface, leading to strong values of PMA. Additional magnetic characteristics are the huge increase of coercive and anisotropy fields in the low temperature regime[48] due to Co(ferromagnetic)-CoO_x antiferromagnetic coupling.

(iii) For the highest employed annealing temperature ($450\,°C$), a $Pt/CoPt/AlO_x$ stack is elaborated

whatever t_{Ox} is. The annealing process overcomes the oxidation mean. Co-O bonds nearly disappear for the benefit of Co-Pt ones. Comparable magnetic and transport signals, at least at room temperature, are consequently recorded for such samples.[23] For instance, as supposed by Rodmacq *et al.*,[23] the reabsorption of oxygen allows full deoxidation of the Co layer (and the appearance of a perpendicular magnetization[49]), and the formation of an optimally oxidized Co/AlO_x interface. The increase of the Hall angle[23] for annealing temperatures between $300\,°C$ and $450\,°C$ is thus simply explained by the replacement of CoO bondings by CoPt ones, according to our study. A scenario is thus given: the most stable location of oxygen in these $Pt/CoPt_x/AlO_x$ trilayers is right at the Co/AlO_x interface, where Co-O-Al bonds can be formed.

In Ref. 50, *ab initio* calculations have shown that the origin of PMA is partially attributed to hybridization between 3d (Co or Fe) and O-2p (MgO) orbitals at the interface between the transition metal and the insulator. The authors have pointed the effect of oxidation conditions on the PMA: over- or underoxidized interfaces reduce PMA values. These theoretical results are validated by our experimental study. They are also in accordance with other published studies related to Co/AlO_x (Ref. 51) and CoFeB/MgO.[52,53] In our samples, the optimized PMA is obtained for a sample with specific characteristics ($t_{Ox} \approx 35 - 40\,s$ and $T_{Ann} \approx 300\,°C$), associated to a weak inter-diffusion between layers. The fundamental role of oxygen with its correlation with the induced perpendicular magnetic anisotropy, or other fundamental magnetic properties such as magneto resistance effects, might be pointed by a combined approach of XRR and XANES.

V. CONCLUSION

Quantitative x-ray reflectivity and x-ray absorption near edge spectroscopy techniques have been combined to study the influence of both annealing temperature and oxidation time in $Pt/Co/AlO_x$ trilayers. The cobalt and aluminum bonds with surrounding atoms are narrowly dependent on T_{Ann} and t_{Ox}. The best geometry is obtained for a stack annealed at $T_{Ann} \approx 300\,°C$ and oxidized during $t_{Ox} \approx 35-40\,s$. They give the best magnetic properties[23] at room temperature. The benefits of combining local and non local techniques are demonstrated. Strategies for future research on these systems, merging metals and oxides, should lead to a fine-tuning architecture with appropriate composition and annealing, in the aim to optimize the functional magnetic properties.

ACKNOWLEDGMENTS

[1]M. Julliere, Phys. Lett. A **54**, 225 (1975).

[2]S. Mao, J. Nanosci. Nanotechnol. **7**, 4084 (2007).

[3]Y. Zheng, Y. Wu, K. Li, J. Qiu, G. Han, Z. Guo, P. Luo, L. An, Z. Liu, L. Wang, S. G. Tan, B. Zong, and B. Liu, J. Nanosci. Nanotechnol. **7**, 4094 (2007).

[4]E. Y. Tsymbal, O. N. Mryasov, and P. R. LeClair, J. Phys.: Condens. Matter **15**, R109 (2003).

[5]J. S. Moodera, L. R. Kinder, T. M. Wong, and R. Meservey, Phys. Rev. Lett. **74**, 3273 (1995).

[6]S. S. P. Parkin, C. Kaiser, A. Panchula, P. M. Rice, B. Hughes, M. Samant, and S.-H. Yang, Nature Mater. **3**, 862 (2004).

[7]H. X. Wei, Q. H. Qin, M. Ma, R. Sharif, and X. F. Han, J. Appl. Phys. **101**, 09B501 (2007).

[8]J. Hayakawaa, S. Ikeda, Y. M. Lee, F. Matsukura, and H. Ohno, Appl. Phys. Lett. **89**, 232510 (2006).

[9]M. Sharma, S. X. Wang, and J. H. Nickel, Phys. Rev. Lett. **82**, 616 (1999); J. M. De Teresa, A. Barthélémy, A. Fert, J. P. Contour, F. Montaigne, and P. Seneor, Science **286**, 507 (1999).

[10]C. H. Shang, J. Nowak, R. Jansen, and J. S. Moodera, Phys. Rev. B **58**, R2917 (1998).

[11]R. Jansen and J. S. Moodera, J. Appl. Phys. **83**, 6682 (1998).

[12]E. Y. Tsymbal and D. G. Pettifor, J. Appl. Phys. **85**, 5801 (1999).

[13]J. Nassar, M. Hehn, A. Vaures, F. Petroff, and A. Fert, Appl. Phys. Lett. **73**, 698 (1998).

[14]M. Sato, H. Kikuchi, and K. Koayashi, J. Appl. Phys. **83**, 6691 (1998).

[15]W. Oepts, M. F. Gillies, R. Coehoorn, R. J. M. Van de Veerdonk, and W. J. M. De Jonge, J. Appl. Phys. **89**, 8038 (2001).

[16]A. K. Petford-Long, Y. Q. Ma, A. Cerezo, D. J. Larson, E. W. Singleton, and B. W. Karr, J. Appl. Phys. **98**, 124904 (2005).

[17]C. G. C. H. M. Fabrie, J. T. Kohlhepp, H. J. M. Swagten, B. Koopmans, and W. J. M. De Jonge, J. Appl. Phys. **99**, 08T303 (2006).

[18]J. C. A. Huang and C. Y. Hsu, J. Appl. Phys. **98**, 064901 (2005).

[19]P. H. P. Koller, F. W. M. Vanhelmont, H. Boeve, R. Coehoorn, and W. J. M. de Jonge, J. Appl. Phys. **93**, 8549 (2003).

[20]N. D. Telling, G. Van Der Laan, S. Ladak, R. J. Hicken, and E. Arenholz, J. Appl. Phys. **99**, 08E505 (2006).

[21]C. Martínez Boubeta, C. Clavero, J. M. García-Martín, G. Armelles, A. Cebollada, Ll. Balcells, J. L. Menéndez, F. Peiró, A. Cornet, and M. F. Toney, Phys. Rev. B **71**, 014407 (2005).

[22]J. C. A. Huang, C. H. Lee, and K. L. Yu, J. Appl. Phys. **89**, 7059 (2001).

[23]B. Rodmacq, A. Manchon, C. Ducruet, S. Auffret, and B. Dieny, Phys. Rev. B **79**, 024423 (2009).

[24]A. Manchon, S. Pizzini, J. Vogel, V. Uhlir, L. Lombard, C. Ducruet, S. Auffret, B. Rodmacq, B. Dieny, M. Hochstrasser, and G. Panaccione, J. Appl. Phys. **103**, 07A912 (2008).

[25]F. Fettar, H. Garad, L. Ortega, A. Y. Ramos, P. Bazawilski, P. Plaindoux, S. Auffret, B. Rodmacq, and B. Dieny, IEEE Trans. Magn. **45**, 3905 (2009).

[26]H. Garad, L. Ortega, A. Y. Ramos, J. Marcus, F. Gay, F. Fettar, S. Auffret, B. Rodmacq, and B. Dieny, J. Appl. Phys. **109**, 07C117 (2011).

[27]DIFFRAC PLUS LEPTOS Analytical Software for XRD and XRR, Bruker Advanced x-ray Solutions, 2004; A. Ulyanenkov, Appl. Surf. Sci. **253**, 106 (2006).

[28]L. G. Parratt, Phys. Rev. **95**, 359 (1954).

[29]J. Kim, J.-W. Lee, J.-R. Jeong, S.-C. Shin, Y. H. Ha, Y. Park, and D. W. Moon, Phys. Rev. B **65**, 104428 (2002).

[30]C. Train, P. Beauvillain, V. Mathet, G. Penissard, and P. Veillet, J. Appl. Phys. **86**, 3165 (1999).

[31]A. Quade and H. Wulff, Thin Solid Films **355–356**, 494 (1999).

[32]S. A. Correa, G. G. Marmitt, N. M. Bom, A. T. da Rosa, F. C. Stedile, C. Radtke, G. V. Soares, I. J. R. Baumvol, C. Krug, and A. L. Gobbi, Appl. Phys. Lett. **95**, 051916 (2009).

[33]M. Raju, S. Chaudhary, and D. K. Pandyaa, Appl. Phys. Lett. **98**, 212506 (2011).

[34]A. T. G. Pym, A. Lamperti, B. K. Tannera, T. Dimopoulos, M. Rhrig, and J. Wecker, Appl. Phys. Lett. **88**, 162505 (2006).

[35]J. D. R. Buchanan, T. P. A. Hase, B. K. Tanner, N. D. Hughes, and R. J. Hicken, Appl. Phys. Lett. **81**, 751 (2002).

[36]A. Velosoa, P. P. Freitas, P. Wei, N. P. Barradas, J. C. Soares, B. Almeida, and J. B. Sousa, Appl. Phys. Lett. **77**, 1020 (2000).

[37]Y. Li and S. X. Wanga, J. Appl. Phys. **91**, 7950 (2002).

[38]M. Vadalá, K. Zhernenkov, M. Wolff, B. P. Toperverg, K. Westerholt, H. Zabel, P. Wisniowski, S. Cardoso, and P. P. Freitas, J. Appl. Phys. **105**, 113911 (2009).

[39]O. Bezencenet, H. Magnan, C. Mocuta, E. Fonda, S. Stanescu, P. Ohresser, R. Belkhou, and A. Barbier, Phys. Rev. B **81**, 085419 (2010).

[40]Y. Joly, Phys. Rev. B **63**, 125120 (2001).

[41]Y. S. Lee, J. Y. Rhee, C. N. Whang, and Y. P. Lee, Phys. Rev. B **68**, 235111 (2003).

[42]S. Couet, K. Schlage, K. Saksl, and R. Rohlsberger, Phys. Rev. Lett. **101**, 056101 (2008).

[43]M. Gonzalez-Silveira, J. Rodriguez-Viejo, M. T. Clavaguera-Mora, T. Bigault, and J. L. Lábár, Phys. Rev. B **75**, 075419 (2007).

[44]H. Chen and S. M. Heald, J. Appl. Phys. **66**, 1793 (1989).

[45]M.-H. Cho, Y. S. Roh, C. N. Whang, K. Jeong, H. J. Choi, S. W. Nam, D.-H. Ko, J. H. Lee, N. I. Lee, and K. Fujihara, Appl. Phys. Lett. **81**, 1071 (2002).

[46]S. Couet, K. Schlage, K. Saksl, and R. Rohlsberger, Phys. Rev. B **79**, 085417 (2009).

[47]D. Kim, J. E. Saal, L. Zhou, S. Shang, Y. Du, and Z.-K. Li, CALPHAD: Comput. Coupling Phase Diagrams Thermochem. **35**, 323 (2011).

[48]H. Garad, L. Ortega, J. Marcus, F. Gay, F. Fettar, S. Auffret, B. Rodmacq, and B. Dieny, "Modeling of the temperature dependence of coercive field in Pt/Co/AlO$_x$," Appl. Phys. Lett. (to be published).

[49]J. H. Lee, D. H. Im, C. S. Yoon, C. K. Kim, Y. Ando, H. Kubota, and T. Miyazaki, J. Appl. Phys. **94**, 7778 (2003).

[50]H. X. Yang, M. Chshiev, B. Dieny, J. H. Lee, A. Manchon, and K. H. Shin, Phys. Rev. B **84**, 054401 (2011).

[51]D. Lacour, M. Hehn, M. Alnot, F. Montaigne, F. Greullet, G. Lengaigne, O. Lenoble, S. Robert, and A. Schuhl, Appl. Phys. Lett. **90**, 192506 (2007).

[52]S. Ikeda, K. Miura, H. Yamamoto, K. Mizunuma, H. D. Gan, M. Endo, S. Kanai, J. Hayakawa, F. Matsukura, and H. Ohno, Nature Mater. **9**, 721 (2010).

[53]M. Endo, S. Kanai, S. Ikeda, F. Matsukura, and H. Ohno, Appl. Phys. Lett. **96**, 212503 (2010).